Phase transitions in an adaptive network with the global order parameter adaptation

M. Manoranjani,[1] V. R. Saiprasad,[1] R. Gopal,[1] D. V. Senthilkumar,[2,*] and V. K. Chandrasekar[1,†]

[1]*Department of Physics, Centre for Nonlinear Science and Engineering, School of Electrical and Electronics Engineering, SASTRA Deemed University, Thanjavur 613 401, India*

[2]*School of Physics, Indian Institute of Science Education and Research, Thiruvananthapuram-695016, India*

(Received 29 June 2023; accepted 29 September 2023; published 13 October 2023)

We consider an adaptive network of Kuramoto oscillators with purely dyadic coupling, where the adaptation is proportional to the degree of the global order parameter. We find only the continuous transition to synchronization via the pitchfork bifurcation, an abrupt synchronization (desynchronization) transition via the pitchfork (saddle-node) bifurcation resulting in the bistable region R_1. This is a smooth continuous transition to a weakly synchronized state via the pitchfork bifurcation followed by a subsequent abrupt transition to a strongly synchronized state via a second saddle-node bifurcation along with an abrupt desynchronization transition via the first saddle-node bifurcation resulting in the bistable region R_2 between the weak and strong synchronization. The transition goes from the bistable region R_1 to the bistable region R_2, and transition from the incoherent state to the bistable region R_2 as a function of the coupling strength for various ranges of the degree of the global order parameter and the adaptive coupling strength. We also find that the phase-lag parameter enlarges the spread of the weakly synchronized state and the bistable states R_1 and R_2 to a large region of the parameter space. We also derive the low-dimensional evolution equations for the global order parameters using the Ott-Antonsen ansatz. Further, we also deduce the pitchfork, first and second saddle-node bifurcation conditions, which is in agreement with the simulation results.

DOI: 10.1103/PhysRevE.108.044307

I. INTRODUCTION

Adaptive networks are largely characterized by self-adaption of either their connections, altering their structure, or their connection weights in congruence with their nodal dynamics [1]. Recent investigations on the adaptive networks have unraveled a a plethora of complex collective macroscopic dynamical states that are peculiar to the adaptation rules [2–16]. For instance, splay states and antipodal clusters in multiplex networks [2], hierarchical multilayered structures [3], including a certain mesoscale structures [4,5] are found to be exclusive features of the adaptivity of the employed networks. Very recently an adaptive network was found to facilitate a single-step and a sequence of multistage transitions to synchronization based on the nature of the defects prevailing in the intrinsic frequencies of the adaptively coupled phase oscillators [6]. Itinerant chimeras characterized by a short and a long durations of coherent epochs are reported in adaptive networks with coevolving connection weights and phases of the oscillators under an external forcing [7]. Adaptive couplings have also been employed in networks with higher-order interactions (simplicial complexes) and found to facilitate the onset of abrupt synchronization [8,9] and abrupt desynchronization [10,11].

Typically, the connection weights k_{ij} for the pairwise (dyadic) interactions evolve in accordance with the evolution equation $\dot{k}_{ij} = \varepsilon \sin(\theta_i - \theta_j + \beta)$, where ε is the coupling strength, θ_i and θ_j are the phases of the i^{th} and j^{th} oscillators and β is the asymmetry parameter. Note that the connection weights coevolve with the phases of the oscillators. Depending on the value of β, the adaptation rule for k_{ij} turns out to be spike-time dependent plasticity (STDP) [17,18], Hebbian and anti-Hebbian [19]. Another plasticity rule called structural plasticity (SP), operating on a longer time scale compared to STDP, involves the addition and elimination of the synaptic contacts, which could be activity-dependent [20,21]. Studies of SP with homeostatic mechanisms have been used to study specific brain functions. The homeostatic SP is essential for stabilizing the neuronal networks by scaling the synaptic weights and by adding and removing contacts [22,23]. In contrast, heterosynaptic plasticity has been reported in various situations where the strength of the synapse between neurons is modified due to the response of the other neurons [24–26]

Recently, an adaptive coupling was employed for a pure simplicial complexes and elucidated that Hebbian plasticity rule abrupt desynchronization [10]. In particular, purely triadic (two-simplex) coupling was considered along with the connection weights k_{ijl} with the evolution equation $\dot{k}_{ijl} = \varepsilon \sin(\theta_j + \theta_l - 2\theta_i + \beta)$. The influence of both the dyadic and triadic adaptive couplings on the synchronization transition has also been investigated [8]. The local connection weights k_{ij} and k_{ijl} evolve in accordance with the phases of the particular pair or group of oscillators constituting the complex (motif). Nevertheless, there are real-world scenarios and applications where the connection weights self-adapts in congruence with the mean field of the population [27]. In particular, the connection weight $k = k_{ij} \propto r^{\alpha}\, \forall\, i, j$, where r is the conventional Kuramoto order parameter, characterizing the mean field of the system under consideration. Such an

*Corresponding author: skumar@iisertvm.ac.in
†Corresponding author: chandru25nld@gmail.com

adaptation of the connection weights with the global order parameter has been studied theoretically [28] and experimentally [29]. Here the coupling strength adapts based on the level of synchronization in the system. Some experiments on Josephson junctions, laser arrays, and mechanical systems suggest that the proposed modifications account for the effective change in the coupling parameter among the oscillators [29]. Very recently, tiered synchronization, characterized by two tiers of weak and strong synchronizations at the interface of abrupt and continuous transition to synchronization, has been reported by adapting the coupling weights, whose amplitude depends on the global order parameter [30]. Weak synchronization is characterized by a small positive value of the global order parameter due to partially entrained oscillators with appreciable drift between them. In contrast, strong synchronization is characterized by a large positive value of the global order parameter due to almost completely entrained oscillators with negligible drift among the latter.

In this work, we consider an adaptive network of Kuramoto oscillators with purely dyadic coupling, where the adaption is proportional to the degree of the global order parameter. We find only the continuous transition to synchronization via the pitchfork bifurcation for small values of the degree of the global order parameter and the adaptive coupling strength. Nevertheless, we find (i) an abrupt synchronization and abrupt desynchronization transitions via the pitchfork and the saddle-node bifurcations, respectively, resulting in the bistable region R_1, (ii) a smooth continuous transition to a weakly synchronized state via the pitchfork bifurcation followed by a subsequent abrupt transition to a strongly synchronized state via a second saddle-node bifurcation along with an abrupt desynchronization transition via the first saddle-node bifurcation resulting in the bistable region R_2 between the weak and strong synchronization, which is being recently reported as tiered synchronization, (iii) transition from the bistable region R_1 to the bistable region R_2, and (iv) transition from the incoherent state to the bistable region R_2 as a function of the coupling strength for intermediate ranges of the degree of the global order parameter and the adaptive coupling strength. Only the continuous transitions from the incoherent state to the synchronized state is observed for the large values of the degree of the global order parameter. We also find that the phase-lag parameter enlarges the spread of the weakly synchronized state and the bistable states R_1 and R_2 to a large region of the parameter space. It is to be noted that the terminologies soft and hard transitions were used [31,32] to refer continuous and abrupt transitions. In this connection, our results display a soft transition to a weak synchronized state and a hard transition to a strong synchronized state. We also derive the low-dimensional evolution equations for the global order parameters using the Ott-Antonsen ansatz. Further, we also deduce the pitchfork, first, and second saddle-node bifurcation conditions, which agree well with the simulation results.

The plan of the paper is as follows. We describe the model and the involved parameters in Sec. II. We deduce the low-dimensional evolution equations for the macroscopic order parameters in Sec. III. We discuss the various observed dynamical states and the accompanied phase transitions along with their bifurcations in Sec. IV. Finally, we will provide the conclusion and discussion in Sec. V.

II. MODEL

The evolution equations for the adaptive network of Kuramoto oscillators, where the connection weights evolve in proportion to the global order parameter, is represented as

$$\dot{\theta}_j = \omega_j + (1 + qr^{\alpha})\left[\frac{k}{N}\sum_{l=1}^{N}\sin(\theta_l - \theta_j + \beta)\right], \quad j = 1, 2, \ldots, N, \tag{1}$$

where θ_j is the phase of the j^{th} oscillator, ω_j is its natural frequency, which is typically assumed to be drawn from a well behaved distribution $g(\omega)$, k is the coupling strength, β is the phase lag (or asymmetry) parameter, the parameter q governs the strength of the adaptation, $r = |1/N\sum_{j=1}^{N} e^{i\theta_j}|$ is the global order parameter, and the power-law exponent α governs the degree of feedback from the global order parameter. Such a type of power-law function for the adaption serves as a typical nonlinear coupling [27–29]. Note that irrespective of the value of α, the adaptive network of Kuramoto oscillators (1) degenerates to the classic Kuramoto model when $q = 0$, whereas $q \neq 0$ results in the desired functional dependence of the coupling on the fraction of the phase-locked oscillators. It also implies that there is no adaptation for $q = 0$. By adjusting the value of q, one is able to control the extent to which the oscillators adapted to the collective behavior of the system.

We consider a unimodal frequency distribution for $g(\omega)$. Specifically, we use the Lorentzian distribution given by

$$g(\omega) = \frac{\gamma}{\pi}\left[\frac{1}{((\omega - \omega_0)^2 + \gamma^2)}\right], \quad \gamma > 0, \tag{2}$$

where γ represents the width parameter of each peak and $\pm\omega_0$ represent the location of the peaks. It is important to note that the distribution $g(\omega)$ is symmetric about ω_0, as given by the equation. This choice of distribution allows us to model the frequency distribution of coupled oscillator systems with a single dominant frequency component, which is often observed in physical systems.

III. EVOLUTION EQUATION OF THE MACROSCOPIC ORDER PARAMETERS

As N, the number of oscillators, approaches infinity, the set of equations (1) can be simplified into a finite set of macroscopic variables. These variables are expressed in terms of the macroscopic order parameters that govern the dynamics of the original system of equations. In the thermodynamic limit, the discrete set of equations can be transformed into a continuous formulation using the probability density function $f(\theta, \omega, t)$. This function characterizes the fraction of oscillators with phases between $[\theta, \theta + d\theta]$ and natural frequency ω at a particular time t. This continuous formulation is useful for analyzing the system dynamics more intuitively and analytically, allowing us to gain much deeper insights into the self-organization of the collective behavior of the network. A period of 2π in θ characterises the periodicity of the distribution $f(\theta, \omega, t)$. It also complies with the following

normalization criterion:

$$\int_0^{2\pi} f(\theta, \omega, t)\, \mathrm{d}\theta = g(\omega)\, \forall\, \omega. \tag{3}$$

The system of equations (1) preserves the total number of oscillators with a given natural frequency ω. The time evolution of the probability density function $f(\theta, \omega, t)$ is governed by the following continuity equation:

$$\frac{\partial f}{\partial t} + \frac{\partial (f v)}{\partial \theta} = 0, \tag{4}$$

where $v(\theta, \omega, t) = \frac{d\theta}{dt}$ is the angular velocity at position θ at time t. From Eq. (1), we can get

$$v(\theta, \omega, t) = \omega + \frac{k(1 + qr^{\alpha})}{2i}[(Ze^{-i(\theta-\beta)} - Z^{\star}e^{i(\theta-\beta)})], \tag{5}$$

where $Z(t) = re^{i\phi}$ is the macroscopic order parameter of the system which is defined as

$$Z = \int_{-\infty}^{\infty} g(\omega) \int_0^{2\pi} f(\theta, \omega, t) e^{i\theta} d\theta d\omega, \tag{6}$$

and $Z^{\star}$ is its complex conjugate. Expanding $f(\theta, \omega, t)$ in the Fourier series and using the Ott-Antonsen ansatz [33,34], one can deduce the following evolution equations for the global order parameters r and ϕ:

$$\dot{r} = -\gamma r - \frac{k}{2}(1 + qr^{\alpha})(r^2 - 1) r \cos(\beta), \tag{7a}$$

$$\dot{\phi} = \omega_0 + \frac{k}{2}(1 + qr^{\alpha})(r^2 + 1) r \sin(\beta). \tag{7b}$$

The system of two coupled nonlinear ordinary differential equations presented above describes the dynamics of the model (1) through its macroscopic variables. The incoherent state is characterized by $r = 0$, while the coherent state is characterized by $r = 1$. The intermediate values of $r \in (0, 1)$ characterizes the degree of entrainment.

IV. RESULTS

We have numerically solved the adaptive network of Kuramoto oscillators (1) using the Runge-Kutta fourth order integration with a step size of 0.01. We have used the Lorentzian distribution for the intrinsic frequency ω_i with $\omega_0 = 0$ and $\gamma = 1$. The number of oscillators is fixed as $N = 10001$, while we vary all the other parameters to uncover their influence on the macroscopic collective dynamical states and the involved phase transitions. We use the time-averaged order parameter R defined as

$$R = \lim_{\tau \to \infty} \frac{1}{\tau} \int_t^{t+\tau} r(t) dt \tag{8}$$

to elucidate the phase transitions as a function of the coupling strength k.

A. Phase transitions for distinct strength of the adaptive coupling

The time-averaged order parameter R is depicted in Fig. 1 for different values of the parameters. To start with, we fix the phase-lag parameter $\beta = 0.0$ and the degree of the global order parameter $\alpha = 2$. For the adaptive coupling strength $q = 1$, one can observe a typical continuous (second-order) phase transition to synchronization, indicated as S, from the incoherent state, indicated as IC, via a pitchfork bifurcation, represented as a solid vertical line [see Fig. 1(a)]. The forward trace is depicted as the line connected by open circles, whereas the backward trace is depicted as the line connected by filled circles, throughout the manuscript unless otherwise specified. Both the forward and reverse traces are made adiabatically. Note that for $q = 0$, only the monostable states are observed in the entire range of the coupling strength k. However, one can observe an additional bistable region between the synchronized state S_1 and IC in the range of $k \in (1.25, 2)$ for larger values of the adaptive coupling strength as depicted in Fig. 1(b) for $q = 3.8$. It is to be noted that the phase transitions in Fig. 1(b) are not continuous in the bistable region but emerge as abrupt transitions via the pitchfork bifurcation and the saddle-node bifurcation, indicated by dashed vertical line, during the forward and reverse traces, respectively. The abrupt desynchronization transition manifests via the saddle-node bifurcation ($SN1$) during the reverse trace, whereas the abrupt synchronization transition to S_1 manifests via the pitchfork bifurcation (PF) during the forward trace. Thus, it is evident that large adaptive coupling strength facilitates the manifestation of the bistable region $R1$ between S_1 and IC states along with the abrupt synchronization and desynchronization transitions.

Now, we increase the phase-lag parameter to $\beta = 1.0$ to uncover the influence of the phase-lag parameter on the observed dynamical states and their phase transitions in Figs. 1(a) and 1(b). Only the critical value of the onset of the continuous phase transition to synchronization is increased from $k_c = 2.0$ to $k_c = 3.7$ due to the phase-lag parameter for the adaptive coupling strength $q = 1$ [see Fig. 1(c)]. One can also observe the abrupt synchronization and desynchronization transitions in the forward and backward traces along with the bistability between S_1 and IC as in Fig. 1(b) upon increasing the adaptive coupling strength to $q = 3.8$ [see Fig. 1(d)]. Nevertheless, the range of bistable region R_1 is increased to a large extent in the range of $k \in (2.5, 3.7)$ due to the introduction of the phase-lag parameter, elucidating that the latter facilitates the spread of the bistable region to a large extent.

The time-averaged order parameter R is depicted in Fig. 2 for different q and β as a function of k by increasing the degree of the global order parameter to $\alpha = 4$ to understand the influence of α. Now, let us explore the effect of increase in α in the absence of the phase-lag parameter. The first row in Fig. 2 depicts the time-averaged order parameter R for $\beta = 0.0$. A typical second-order transition to synchronization is observed in Fig. 2(a) for $q = 1$ similar to that in Fig. 1(a) despite increase in α. However, two saddle-node bifurcations and the pitchfork bifurcation manifests for $q = 3.8$ mediating the two distinct types of phase transitions [see Fig. 2(b)]. First, there is a continuous transition from IC to the weakly synchronized state S_2 via the PF at $k_c = 2.0$ in a narrow range of $k \in (2.0, 2.2)$ during the forward trace. There is a subsequent abrupt transition from S_2 to strongly synchronized state S_1 at $k_c = 2.2$ via a second saddle-node bifurcation $SN2$, indicated by the dotted-dashed vertical line, during the forward

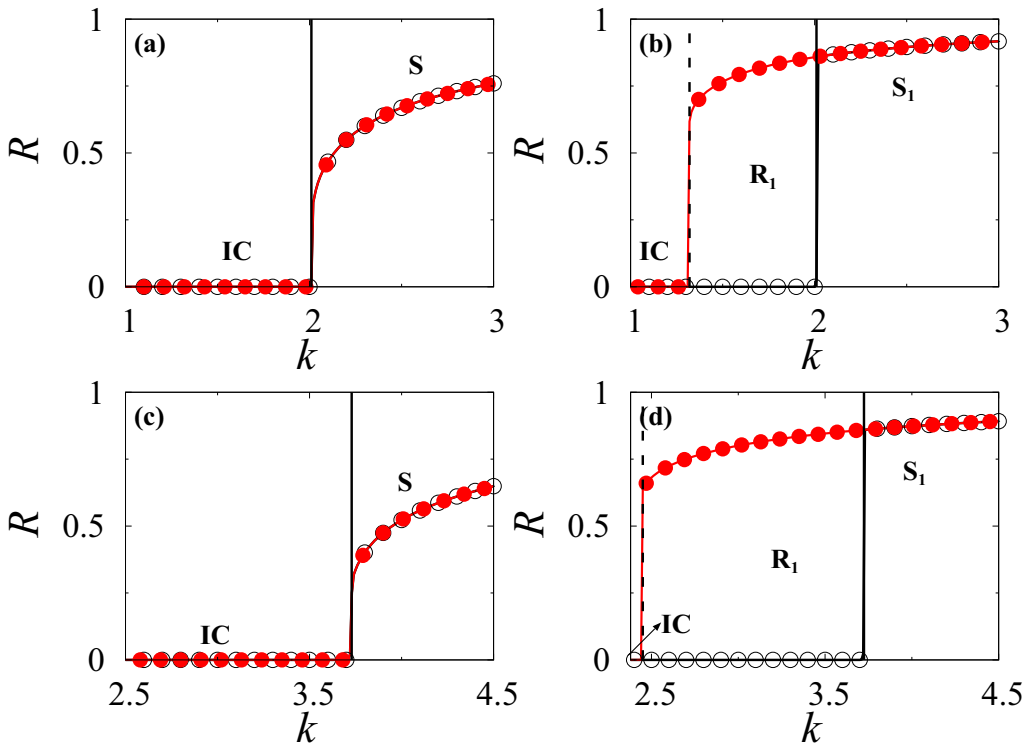

FIG. 1. Time-averaged order parameter (R) illustrating the nature of the phase transitions for $\alpha = 2$ and for different values of the adaptive coupling strength and the phase-lag parameter. (a) and (c) $q = 1$ and (b) and (d) $q = 3.8$. The value of the phase-lag parameter β for (a) and (b) β=0 and (c) and (d) β=1. The lines connected by open and filled circles represent forward and backward traces, respectively. The solid and dashed lines correspond to the pitchfork (10b) and the saddle-node bifurcation (13) conditions, respectively.

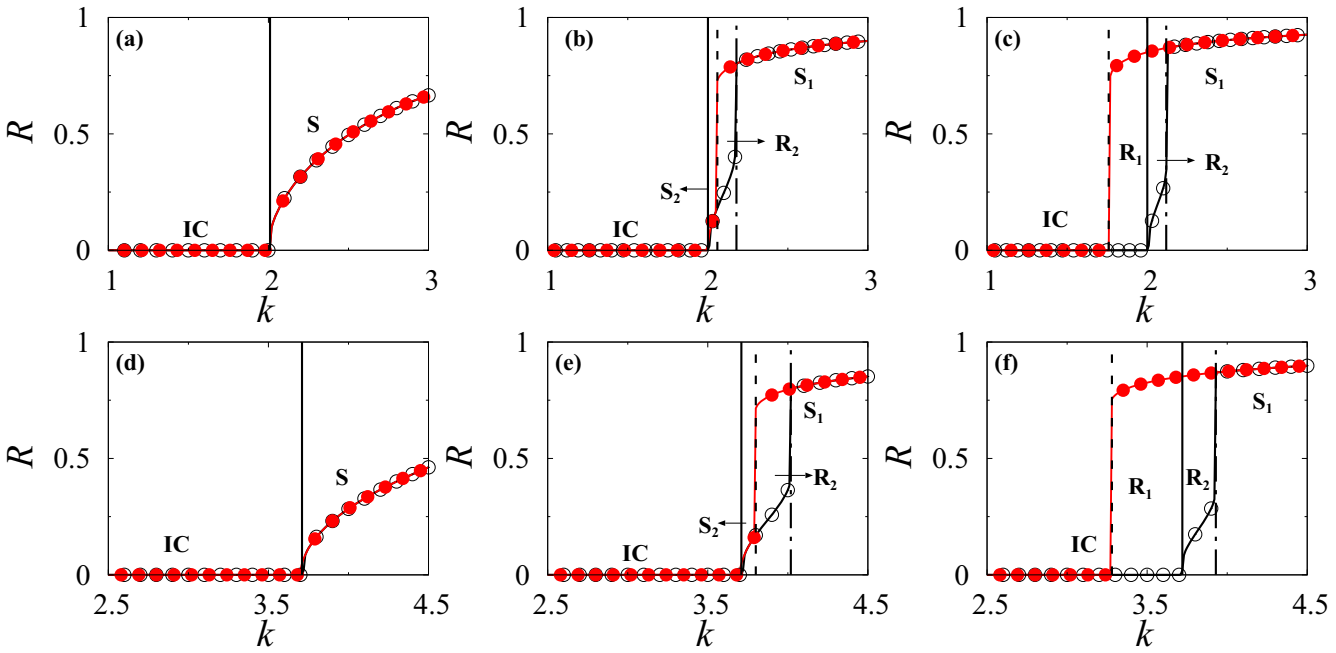

FIG. 2. Time-averaged order parameter (R) illustrating the nature of the phase transitions for $\alpha = 4$ and for different values of the adaptive coupling strength and the phase-lag parameter. (a) and (d) $q = 1$, (b) and (e) $q = 3.8$ and (c) and (f) $q = 5$. The value of the phase-lag parameter β for (a)–(c) β=0 and (d)–(f) β=1. The lines connected by open and filled circles represent forward and backward traces, respectively. The solid, dashed, and dotted-dashed lines correspond to the pitchfork (10b), saddle-node bifurcation ($SN1$) (14a), and the saddle-node bifurcation ($SN2$) (14b) conditions, respectively.

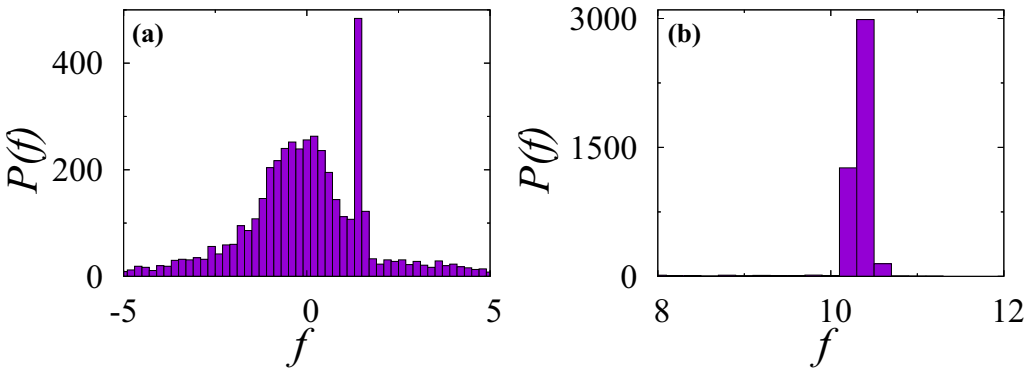

FIG. 3. The frequency distribution is plotted in the bistable region R_2. Plot (a) shows the frequency distribution of weak synchronization state and (b) shows the frequency distribution of strong synchronization state. The parameter values are $q = 5$, $\beta = 1$, $\alpha = 4$ and $k = 3.8$.

trace upon increasing k. The weakly synchronized state S_2 is bounded by PF and $SN2$. The strongly synchronized state S_1 suffers an abrupt desynchronization via the $SN1$ at $k_c = 2.06$ during the reverse trace. The observed phase transitions in Fig. 2(b) result in the second bistable region R_2 between S_1 and S_2 in the range of $k \in (2.06, 2.2)$. One can observe the manifestation of both the bistable regions R_1 and R_2 for yet larger values of the adaptive coupling strength as depicted in Fig. 2(c) for $q = 5$. Note that, here, R_1 is bounded by PF and $SN1$, whereas S_2 and consequently R_2 are bounded by PF and $SN2$.

In the presence of the phase-lag parameter $\beta = 1.0$, one can observe the continuous phase transition with increased k_c for $q = 1$ [see Fig. 2(d)] similar to that in Fig. 1(b). For the adaptive coupling strength $q = 3.8$, the stable range of S_2 is increased in the range of $k \in (3.7, 4.02)$ and consequently, R_2 in the range of $k \in (3.8, 4.02)$ as depicted in Fig. 2(e) for $\beta = 1.0$. Increasing the value of q increases the spread of R_1 and R_2, observed in Fig. 2(c) for $\beta = 0.0$, to a larger range of the coupling strength k as depicted in Fig. 2(f) for $\beta = 1.0$. It is evident that the phase-lag parameter essentially increases k_c and facilitates the spread of S_2 and the bistable regions R_1 and R_2, while the large values of adaptive coupling strength results in the manifestation of S_2 and the abrupt synchronization and desynchronization transitions via appropriate bifurcations.

Note that the coexisting weak and strong synchronizations in the bistable region R_2 have been recently reported as tiered-synchronization [30,35]. In addition, the so-called Bellerophon states have similar signatures but are characterized by quantized clusters at S_2 without any phase and frequency entrainments instead with the same average velocity among the clusters [36,37]. It is also to be noted that both weak and strong synchronization in the region R_2 in Fig. 2 is characterized by suitably entrained phase oscillators as quantified by the time-averaged order parameter R, thereby elucidating the region R_2 is distinctly different from the Bellerophon states though share quantitatively similar signatures but with distinct microscopic structures. To corroborate it, the frequency distributions of both weak and strong synchronizations in the bistable region R_2 are depicted in Figs. 3(a) and 3(b), respectively. The partial entrainment of the frequencies of the oscillators with frequency drift among them and almost complete entrainment of the frequencies of the oscillators with negligible drift is clearly evident from Figs. 3(a) and 3(b), respectively. We have also depicted the attractors at the incoherent state [Figs. 4(a) and 4(d)], weakly synchronized state [Figs. 4(b) and 4(e)], and strongly synchronized state [Figs. 4(c) and 4(f)] corresponding to both the reduced system of Eqs. (7) in the first row and the original discrete system of adaptively coupled Kuramoto oscillators Eq. (1) in the second row.

Two parameter phase diagrams in the (k, q) parameter space is depicted in Fig. 5 for two different α and β for a global perspective of the observed phase transitions. The phase diagram for $\alpha = 2$ and $\beta = 0.0$ is depicted in Fig. 5(a). For small values of the adaptive coupling strength q, there is a continuous transition from IC to the synchronized state S via the PF (solid line) as a function of k as observed in the first column of Figs. 1 and 2. For $q > 1$, there is an abrupt synchronization transition to S_1 via the PF in the forward trace, which suffers an abrupt desynchronization transition in the reverse trace via $SN1$ (dashed line) as shown in the second column of Fig. 1. Consequently, the bistable region R_1 is enclosed between the $SN1$ and PF bifurcations. The stability condition for the incoherent state, which results in the pitch-fork bifurcation, is obtained, through the linear stability analysis of Eq. (7a) about $r = 0$, as

$$\lambda = -v + \frac{k}{2}(1 + qr^{\alpha})\cos(\beta) \tag{9}$$

as a function of the phase-lag parameter α. Depending upon the value of α, two PF bifurcation curves can be deduced from Eq. (9) as

$$k_{PF} = \frac{2v\sec(\beta)}{(1+q)}, \quad \alpha = 0, \tag{10a}$$

$$k_{PF} = 2v\sec(\beta), \quad \alpha > 0. \tag{10b}$$

The stability condition for the synchronized steady state S_1 results in condition for the $SN1$ bifurcation, which can be deduced from Eq. (7a) for various α value. The evolution equation for r (7a) can be set to zero, as the synchronized state is characterized by a finite time-independent value of r, to obtain the solution corresponding to the synchronized state. Note that it is not possible to deduce the synchronized solution for an arbitrary α. Nevertheless, one can deduce the synchronized solution for a specific value of α. For $\alpha = 2$

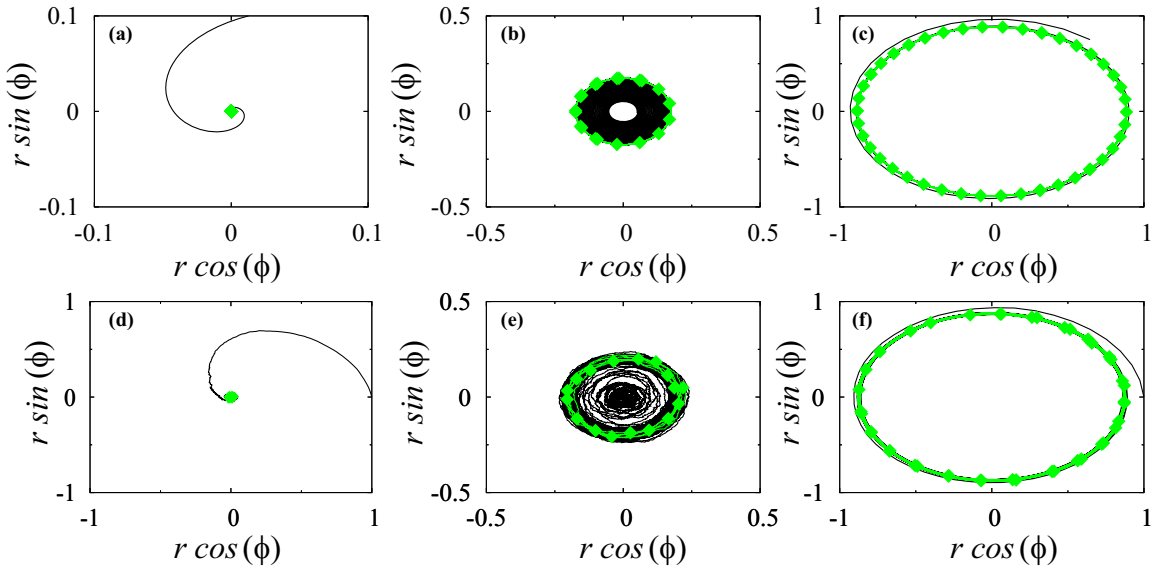

FIG. 4. (a)–(c) Attractors of the reduced system (7) in different regions and (d)–(f) attractors of the original system (1) in different regions. The parameters are $q = 5, \alpha = 4$ and $\beta = 1$. The fixed point attractor corresponding to the incoherent state is plotted for $k = 1$ in (a) and (d). The attractor corresponding to the weak synchronized state is plotted for $k = 3.8$ in (b) and (e). The attractor corresponding to the strong synchronized state is plotted for $k = 4.2$ in (c) and (f). The solid black line indicates the transient trajectory and the line connected with filled diamond represents the stable attractor.

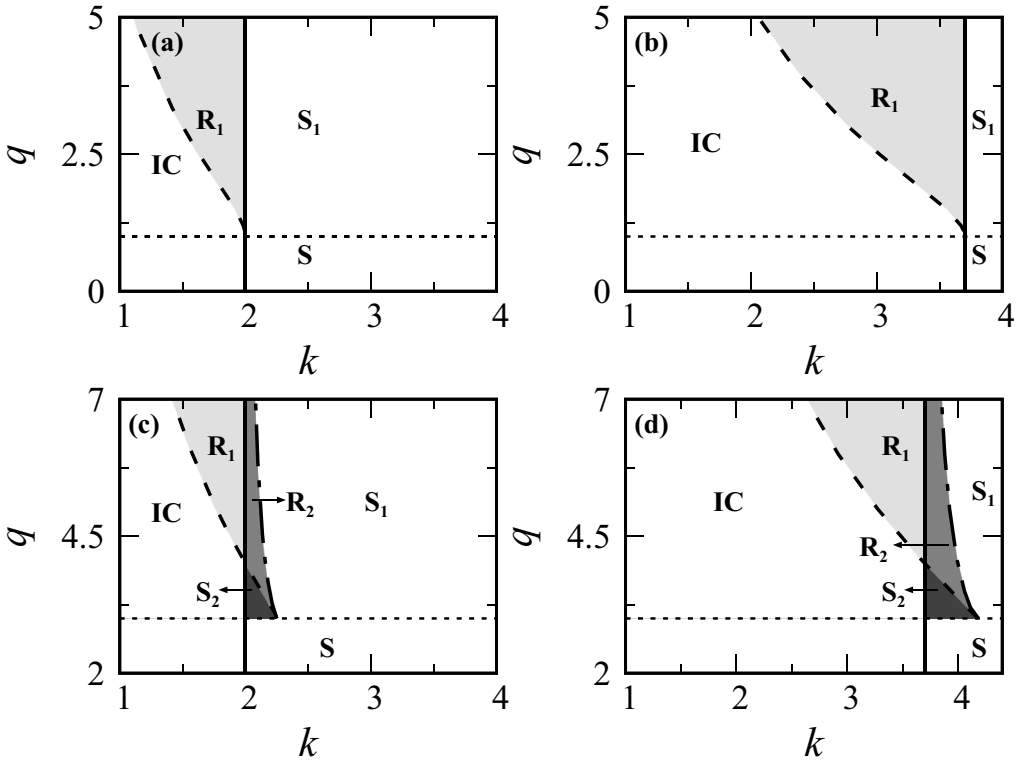

FIG. 5. Two parameter phase diagrams in the (k, q) parameter space for different α and β. (a) and (b) $\alpha = 2$ and (c) and (d) $\alpha = 4$. The value of the phase-lag parameter β for (a) and (c)=0 and (b) and (d)=1. The solid, dashed, and dotted-dashed lines correspond to the pitchfork (10b), saddle-node bifurcation ($SN1$) (14a) and the saddle-node bifurcation ($SN2$) (14b) conditions, respectively.

Eq. (7a) can be written as,

$$r^4 kq\cos(\beta) - r^2 k\cos(\beta)(q-1) + 2\gamma - k\cos(\beta) = 0. \tag{11}$$

The synchronized solution is obtained from the above equation as

$$r_s = \sqrt{\frac{1}{2q}\left(\frac{\sqrt{k(q+1)^2\cos(\alpha) - 8\gamma q}}{\sqrt{k}\sqrt{\cos(\alpha)}} + q - 1\right)}. \tag{12}$$

Now, the linear stability analysis of Eq. (7a) about r_s results in the stability condition for S_1 as

$$k_{SN1} = \frac{8\gamma q\sec(\beta)}{(q+1)^2}. \tag{13}$$

A similar approach is used to deduce the stability condition of $SN1$ for different α values. The solid and the dashed lines in Figs. 1–5 are indeed obtained from the analytical pitchfork (10b) and saddle-node (13) bifurcation conditions, while the shaded regions and the regions indicated by IC, S and S_1 in Fig. 5 are obtained from the original evolution equations corresponding to the adaptive network of Kuramoto oscillators, Eq. (1). The horizontal dotted line at $q = 1$ is obtained by equating Eqs. (10b) and (13), which demarcates the range of q leading to the continuous transition to S and the abrupt synchronization transition to S_1 and its desynchronization transition.

Two phase diagrams for $\alpha = 2$ and $\beta = 1.0$ are depicted in Fig. 5(b), in which the observed dynamical states, bifurcations and bistability are similar to that in Fig. 5(a) for $\beta = 0.0$. Note that the transition from continuous transition to S to the abrupt synchronization transition to S_1 manifests again at $q = 1$, similar to that in Fig. 5(a), which is independent of β. However, the presence of the phase-lag parameter increases the value of $k_c = k_{PF}$ as elucidated in Figs. 1 and 2. In addition, the spread of the bistable region R_1 is also increased to a large extent [compare Figs. 5(a) and 5(b)]. Yet further increase in α facilitates the manifestation of S_2 and R_2 via $SN2$ in the phase diagram as depicted in Fig. 5(c) for $\alpha = 4$ and $\beta = 0.0$. The PF bifurcation condition is the same as in Eq. (10b). The stability of the synchronized steady states S_1 and S_2 results in the saddle-node bifurcation conditions for $\alpha = 4$ as

$$k_{SN1} = \frac{2\gamma(q\cos(\beta)(q+9) - \sqrt{F_2})}{\cos(2\beta)(1+q^2+2q) + (q+1)^2}, \tag{14a}$$

$$k_{SN2} = \frac{2\gamma(q\cos(\beta)(q+9) + \sqrt{F_2})}{\cos(2\beta)(1+q^2+2q) + (q+1)^2}, \tag{14b}$$

where $F_2 = q\cos^2(\beta)(q^3 - 9q^2 + 27q - 27)$. The dashed and dotted-dashed lines in Fig. 5(c) are indeed the saddle-node bifurcation conditions k_{SN1} and k_{SN2}, respectively. Equating the pitchfork bifurcation condition, Eq. (10b), and the above saddle-node condition leads to the condition $q = 3$ (dotted horizontal line), which demarcates the range of q leading to the continuous and the abrupt synchronization and desynchronization transitions in Fig. 5(c). Now, the phase-lag parameter for $\alpha = 4$ enlarges the spread of S_2 and the bistable regions R_1 and R_2 in the two parameter phase diagram as shown in Fig. 5(d) for $\beta = 1.0$, otherwise, the dynamical states, bistable states, phase transitions and the involved bifurcations remain unaltered from that in Fig. 5(c). However, note that k_{PF} is increased due to β in consistent with that in Figs. 1 and 2.

B. Phase transitions for distinct degree of the global order parameter

The phase transitions that have been analyzed so far are for just two discrete values of α. In order to understand the phase transitions as a function of the parameter that characterizes the degree of the global order parameter, we analyze the phase transitions as a function of α. The time-averaged order parameter R is depicted in Fig. 6 for different α and for fixed $q = 2$ as a function of the coupling strength k. In the absence of the phase-lag parameter, R is depicted in Figs. 6(a) and 6(b) for $\alpha = 1$ and $\alpha = 3$, respectively. One can observe an abrupt synchronization(desynchronization) transition via the $PF(SN1)$ bifurcation in the forward(reverse) trace, and the bistability R_1 between IC and S_1 states enclosed by the PF and $SN1$ bifurcation curves. Only a continuous synchronization transition is observed in both the forward and reverse traces for $\alpha = 3$ elucidating the emergence of only the monostable states as observed in Figs. 1 and 2 for $\alpha = 2$ and 4, respectively, and for $q = 1$. Note that k_{PF} remains independent of α. The phase-lag parameter simply enlarges the spread of the bistable region R_1 [see Fig. 6(c)] for $\alpha = 1.0$ and $\beta = 1.0$ with a larger $k_{PF} = 3.7$. The phase transition for $\alpha = 3$ in Fig. 6(d) remains unchanged from Fig. 6(b) except for increase in $k_{PF} = 3.7$ in the presence of the phase-lag parameter. The pitchfork bifurcation condition remains the same as in Eq. (10b), whereas the stability condition pertaining to $SN1$ for $\alpha = 1$ can be deduced as

$$k_{SN1} = \frac{\cos(\beta)(\gamma - 9\gamma q^2) + \sqrt{F_1}}{\cos^2(\beta)(1 + q^4 - 2q^2)}, \tag{15}$$

where $F_1 = \gamma^2\cos^2(\beta)(1 + 27q^6 + 27q^4 + 9q^2)$. For $\alpha = 3$, the stability for the synchronized steady state S_1 results in polynomial equation in k as

$$27k_{SN1}^3(q^2-1)^2\cos^3(\beta) - 54\gamma k_{SN1}^2 q^2(q^2-25)\cos^2(\beta) - 5625\gamma^2 k_{SN1} q^2\cos(\beta) + 6250\gamma^3 q^2 = 0. \tag{16}$$

The root of the above polynomial equation gives the stability condition for $SN1$. Note that the solid and the dashed lines in Fig. 6 are the analytical stability curves corresponding to PF and $SN1$ bifurcations. Comparing the results in Figs. 1 and 2 with that in Fig. 6, it is evident that suitable choices of (q, α) results in the continuous and abrupt synchronization/desynchronization transitions.

The time-averaged order parameter R is depicted for increasing value of α and for $q = 4$ as a function of the coupling strength k in Fig. 7. Phase transitions for both the forward and reverse traces are shown in the first row of Fig. 7 in the absence of the phase-lag parameter, $\beta = 0$. The dynamical states and their phase transitions in Fig. 7(a) for $\alpha = 2$ are similar to those observed in Fig. 6(a), where the phase transitions are observed only via PF and $SN1$. Nevertheless, the synchronized S_2 manifests between PF and $SN2$ in a rather narrow range of k for $\alpha = 3.5$ [see Fig. 7(b)] resulting in R_2 in addition to the dynamical states and phase transitions in Fig. 7(a). For yet

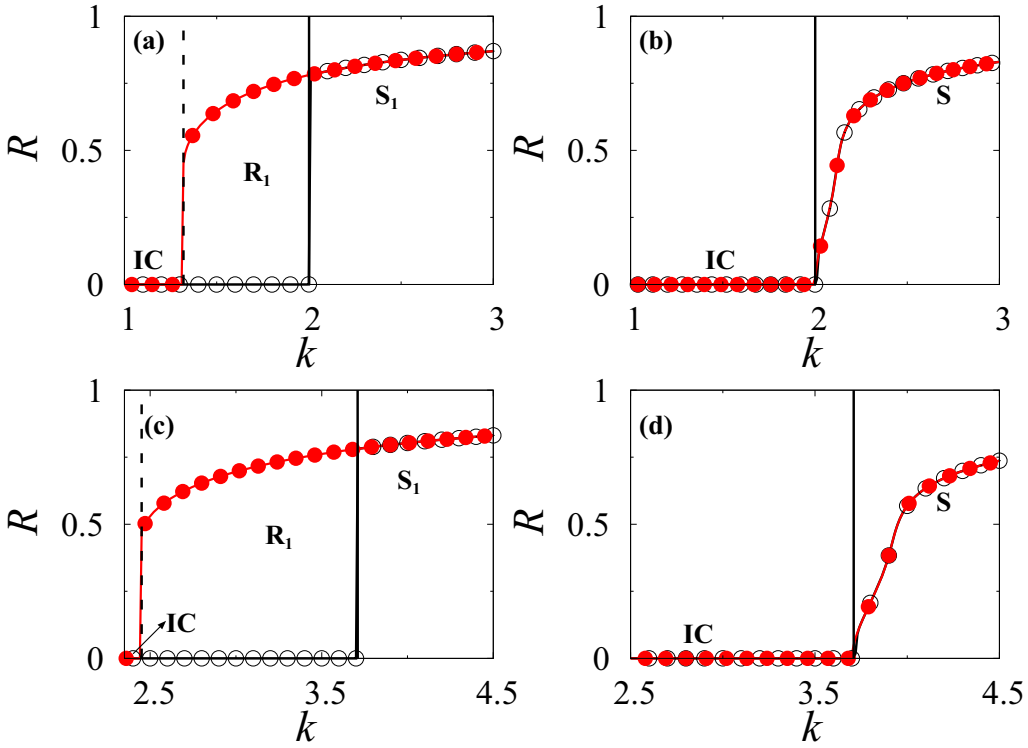

FIG. 6. Time-averaged order parameter (R) illustrating the nature of the dynamical transitions for $q = 2$ and for different values of the degree of global order parameter and the phase-lag parameter. (a) and (c) $\alpha = 1$ and (b) and (d) $\alpha = 3$. The value of the phase-lag parameter β for (a) and (b) $\beta = 0$ and (c) and (d) $\beta = 1$. The lines connected with open and filled circles represent forward and backward traces, respectively. The solid, and dashed lines correspond to the pitchfork (10b), saddle-node bifurcation ($SN1$) (15) conditions, respectively.

larger α, $SN1$ and $SN2$ shift towards the larger k resulting in a large range of a stable S_2 state as a function of k as depicted in Fig. 7(c) for $\alpha = 5$ and retaining the bistable region R_2 in the rather narrow range of k. For $\alpha = 7$, only a continuous transition to synchronization is observed in both the forward and reverse traces [see Fig. 7(d)]. Thus, only an intermediate

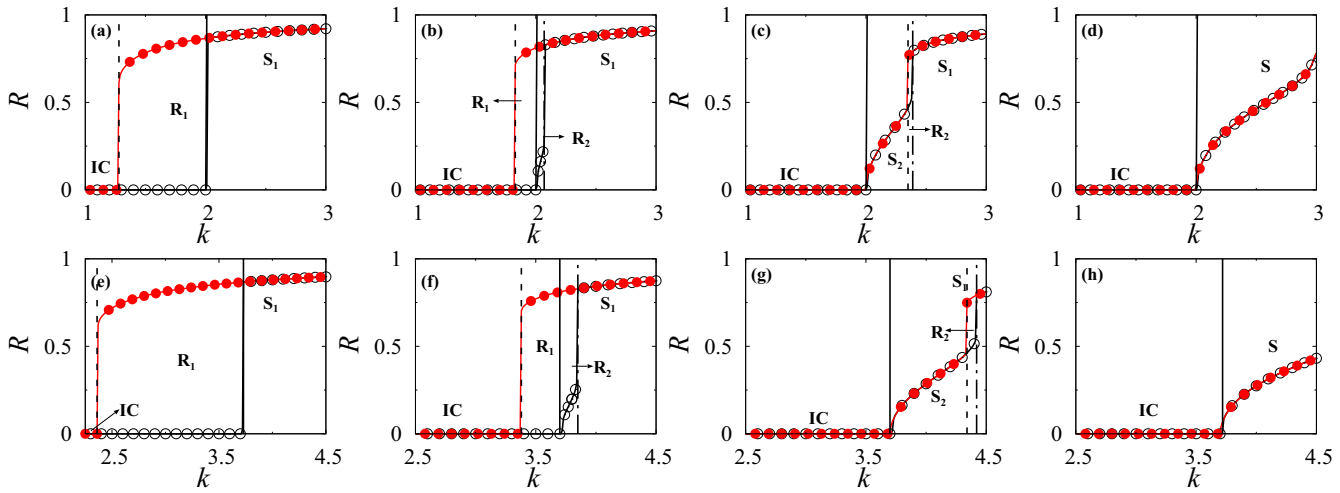

FIG. 7. Time-averaged order parameter (R) illustrating the nature of the dynamical transitions for $q = 4$ and for different values of the degree of global order parameter and the phase-lag parameter. (a) and (e) $\alpha = 2$, (b) and (f) $\alpha = 3.5$, (c) and (g) $\alpha = 5$ and (d) and (h) $\alpha = 7$. The value of the phase-lag parameter β for (a)–(d) $\beta = 0$ and (e)–(h) $\beta = 1$. The lines connected with open and filled circles represent forward and backward traces, respectively. The solid, dashed, and dotted-dashed lines correspond to the pitchfork (10b), saddle-node bifurcation ($SN1$), and the saddle-node bifurcation ($SN2$) conditions, respectively.

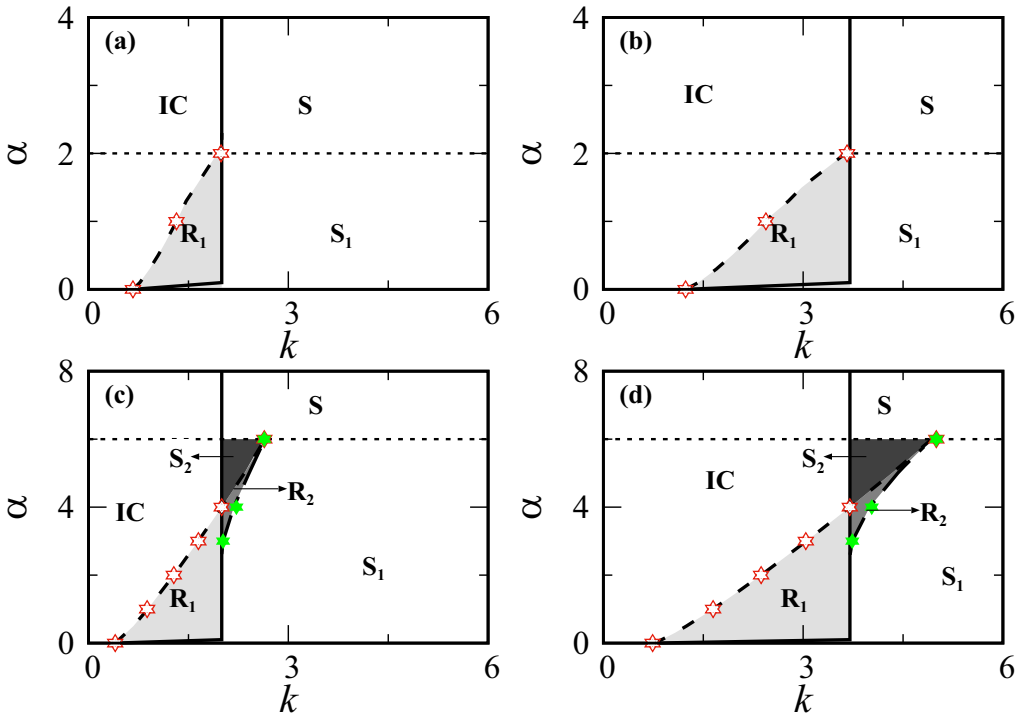

FIG. 8. Two parameter phase diagrams in the (k, α) parameter space for different q and β. (a) and (b) $q = 2$ and (c) and (d) $q = 4$. The value of the phase-lag parameter β for (a) and (c) $\beta = 0$ and (b) and (d) $\beta = 1$. The pitchfork bifurcation is represented as solid line. The first and second saddle node bifurcations are represented as dotted and dashed-dotted lines, respectively.

value of the degree of the global order parameter facilitates the manifestation of S_2 state and the bistable states R_1 and R_2. Furthermore, it is also evident from Figs. 7(a)–7(d) that K_{PF} is independent of α. The solid, dashed, and dotted-dashed vertical lines in Fig. 7 are the analytical stability conditions for the PF, $SN1$, and $SN2$ bifurcations. Phase transitions for both the forward and reverse traces shown in the second row of Fig. 7 for $\beta = 1.0$ are in exact correspondence with that in the first row of Fig. 7 except for an increase in the k_{PF}, S_2 region and bistable states.

Two parameter phase diagrams in the (k, α) parameter space are depicted in Fig. 8 for a global insight on the dynamical transitions. The dynamical states and their boundary curves are similar to those in Fig. 5. Two phase diagrams are depicted in Figs. 8(a) and 8(b) for the phase-lag parameter $\beta = 0.0$ and 1.0, respectively, for $q = 2$. For small values of $\alpha \in (0, 2)$, there is an abrupt synchronization(desynchronization) transition in the forward(backward) trace [see Figs. 8(a) and 8(b)], whereas only a continuous transition to S from IC is observed for $\alpha > 2$. For $\beta = 1$, only the bistable region R_1 is enlarged. One can observe S_2, R_1, and R_2 in the two phase diagrams depicted in Figs. 8(c) and 8(d) for $\beta = 0.0$ and 1.0, respectively, for $q = 4$. The phase transitions are similar to those observed in Figs. 8(a) and 8(b) in the range of $\alpha \in (0, 3)$. There is also a smooth transition to S_2 followed by an abrupt transition to S_1 in a narrow range of $\alpha \in (3, 4)$ in the forward trace as depicted in Fig. 7(b), while there is an abrupt desynchronization transition in the reverse trace. The observed forward transitions are retained in the range of $\alpha \in (4, 6)$, whereas there is an abrupt desynchronization transition to S_2, which is followed by a smooth desynchronization transition to IC state as observed in Fig. 7(c). There exists only a smooth transition to S for $\alpha > 6$. Again the dotted horizontal line can be deduced by equating the PF and $SN2$ conditions. The solid line is the pitchfork bifurcation condition, Eq. (10b), while the lines connected by stars are the $SN1$ and $SN2$ bifurcation conditions. The phase-lag parameter increases the spread of S_2, R_1, and R_2 in Fig. 8(d) without changing the dynamical states and their transitions observed in Fig. 8(c). Note that the transition from continuous transition to S to the abrupt synchronization transition to S_1 manifests at $\alpha = 2$ [see Figs. 8(a) and 8(b)] and at $\alpha = 6$ [see Figs. 8(c) and 8(d)] for $q = 2$ and 4, respectively, which is independent of the phase-lag parameter β.

In the above investigations, we have used only two values of the phase-lag parameter, namely, $\beta = 0.0$ and 1.0. It is evident from the above results that the presence of β facilitates the spread of S_2, R_2 and the range of phase transitions to a large extent. We have depicted the combined width of the bistable regions R_1 and R_2, see Figs. 2(c), 2(f), 6(b), and 6(d) for the width W of the hysteresis enclosed between the two saddle-node bifurcations, in Fig. 9(a) as a function of the phase-lag parameter for different α. For $\beta = 0.0$, smaller(larger) α leads to larger(smaller) width. It is evident from the figure that the combined width increases rapidly(slowly) for smaller(larger) β in the entire explored range of the phase-lag parameter α. Furthermore, k_{PF} increases proportional to the value of β (see Figs. 1–8). The increase in the k_{PF}, defined as $\varepsilon = k_\beta / k_{\beta=0} - 1$, as a function of β is depicted in Fig. 9(b), which illustrates the degree of increase in the critical coupling strength corresponding to the pitch-fork bifurcation.

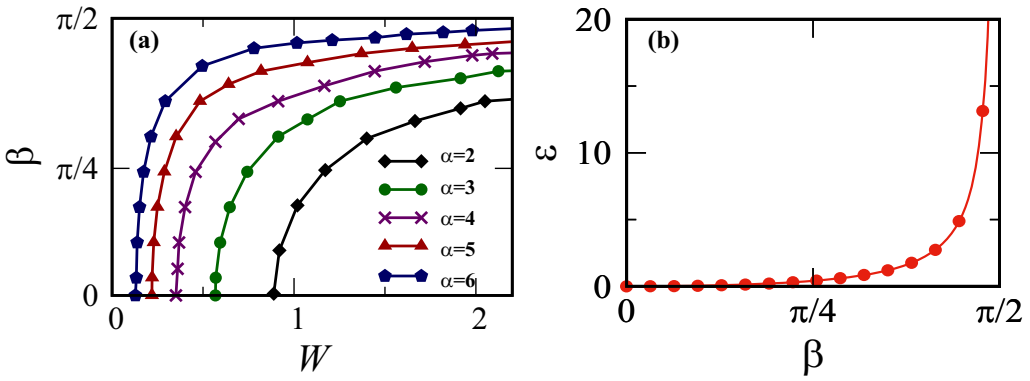

FIG. 9. (a) Width of the bistable state (hysteresis) W for various α. (b) The incoherent region is analyzed with the phase-lag parameter in (ε, β) space and here $\varepsilon = \frac{k_\beta}{k_{\beta=0}} - 1$.

V. CONCLUSION

We have considered an adaptive network of Kuramoto oscillators, where the adaption is proportional to the degree of the global order parameter unlike the STDP, Hebbian, and anti-Hebbian adaption rules. For a low degree of the global order parameter α, low values of the adaptive coupling strength q have simply resulted in the continuous phase transition from the IC state to the S state. However, a large adaptive coupling strength q is found to facilitate the bistable region R_1 between S_1 and IC states along with an abrupt synchronization and an abrupt desynchronization transitions via the pitchfork and the first saddle-node bifurcations, respectively. For intermediate values of α, low values of q have resulted in the continuous transition to S. Nevertheless, we found that the intermediate and large values of q facilitated the manifestation of distinct bistable regions. For an intermediate q, only the bistable state R_2 exists between the two saddle-node bifurcations. Such a bistable state where a weak and strong synchronizations coexist has been recently reported as tiered synchronization. This phenomenon has been so far observed in models with higher-order interactions along with adaptive couplings [30] or with time-delay interactions [35]. In stark contrast we have observed such a state even with a much simpler dyadic adaptive coupling, which is quite interesting. The transition from the incoherent state to the strong synchronization via the relatively weak synchronization is also analogous to the single-step synchronization transition induced by the frequency disorders in an adaptive network of Kuramoto oscillators [6].

Increasing q further resulted in the manifestation of both the bistable states R_1 and R_2 as a function of the coupling strength k. Larger values of α facilitated the manifestation of only the bistable state R_2 other than the continuous transition to S in the entire range of q as a function of k. Yet larger α has resulted only in the continuous transition to S in the entire range of q. Thus, it is evident that the intermediate values of the strength of the adaptive coupling strength and the degree of the global order parameter (feedback) result in the rich dynamical states and their associated phase transitions via appropriate bifurcations. Furthermore, the phase-lag parameter essentially increases k_{PF}, which is found to be independent of α, and facilitates the spread of S_2 and the bistable regions R_1 and R_2 in a large region of the parameter space. The transition from continuous transition to S to the abrupt synchronization transition to S_1 is found to be independent of the phase-lag parameter. We have also deduced the low-dimensional evolution equations for the global order parameters using the Ott-Antonsen ansatz. Further, we have also arrived at the PF, $SN1$, and $SN2$ conditions, which clearly match with the simulation results. We sincerely believe that our results provide much deeper insights on the phase transitions of the adaptive network of Kuramoto oscillators, where the adaptation is proportional to the degree of the global order parameter and also generalizes the results of the adaptive coupling that depends on the local nodal dynamics.

ACKNOWLEDGMENTS

M.M. thanks the Department of Science and Technology, Government of India, for providing financial support through an INSPIRE Fellowship No. DST/INSPIRE Fellowship/2019/IF190871. The work of V.K.C. and R.G. forms part of a research project sponsored by SERB-DST-CRG Project Grant No. C.R.G./2020/004353. R.G. and V.K.C. thanks DST, New Delhi, for computational facilities under the DST-FIST programme (Grant No. SR/FST/PS-1/2020/135) to the Department of Physics. D.V.S. is supported by the DST-SERB-CRG Project under Grant No. CRG/2021/000816.

[1] R. Berner, T. Gross, C. Kuehn, J. Kurths, and S. Yanchuk, Phys. Rep. **1031**, 1 (2023).

[2] R. Berner, J. Sawicki, and E. Schöll, Phys. Rev. Lett. **124**, 088301 (2020).

[3] D. V. Kasatkin, S. Yanchuk, E. Schöll, and V. I. Nekorkin, Phys. Rev. E **96**, 062211 (2017).

[4] R. Gutiérrez, A. Amann, S. Assenza, J. Gómez-Gardeñes, V. Latora, and S. Boccaletti, Phys. Rev. Lett. **107**, 234103 (2011).

[5] E. Pitsik, V. Makarov, D. Kirsanov, N. Frolov, M. Goremyko, X. Li, Z. Wang, A. Hramov, and S. Boccaletti, New J. Phys. **20**, 075004 (2018).
[6] J. Fialkowski, S. Yanchuk, I. M. Sokolov, E. Schöll, G. A. Gottwald, and R. Berner, Phys. Rev. Lett. **130**, 067402 (2023).
[7] S. Thamizharasan, V. K. Chandrasekar, M. Senthilvelan, R. Berner, E. Schöll, and D. V. Senthilkumar, Phys. Rev. E **105**, 034312 (2022).
[8] A. D. Kachhvah and S. Jalan, Phys. Rev. E **105**, L062203 (2022).
[9] S. N. Chowdhury, S. Rakshit, J. M. Buldu, D. Ghosh, and C. Hens, Phys. Rev. E **103**, 032310 (2021).
[10] A. D. Kachhvah and S. Jalan, New J. Phys. **24**, 052002 (2022).
[11] P. S. Skardal and A. Arenas, Phys. Rev. Lett. **122**, 248301 (2019).
[12] Q. Ren and J. Zhao, Phys. Rev. E **76**, 016207 (2007).
[13] S. Y. Ha, S. E. Noh, and J. Park, SIAM J. Appl. Dyn. Syst. **15**, 162 (2016).
[14] R. K. Niyogi and L. Q. English, Phys. Rev. E **80**, 066213 (2009).
[15] P. Seliger, S. C. Young, and L. S. Tsimring, Phys. Rev. E **65**, 041906 (2002).
[16] F. A. Rodrigues, T. K. D. M. Peron, P. Ji, and J. Kurths, Phys. Rep. **610**, 1 (2016).
[17] G. Q. Bi and M. M. Poo, J. Neurosci. **18**, 10464 (1998).
[18] R. Berner, E. Scholl, and S. Yanchuk, SIAM J. Appl. Dyn. Syst. **18**, 2227 (2019)
[19] R. G. M. Morris and D. O. Hebb, *The Organization of Behavior* (Wiley, New York, 1949).
[20] K. Chauhan, A. Khaledi-Nasab, A. B. Neiman, and P. A. Tass, Sci. Rep. **12**, 15003 (2022).
[21] A. V. Ooyen and M. Butz-Ostendorf, *The Rewiring Brain: A Computational Approach to Structural Plasticity in the Adult Brain* (Academic Press, New York, 2017).
[22] M. Butz, F. Wörgötter, and A. van Ooyen, Brain Res. Rev. **60**, 287 (2009).
[23] G. Turrigiano and S. B. Nelson, Nat. Rev. Neurosci. **5**, 97 (2004).
[24] C. B. Picallo and H. Riecke, Phys. Rev. E **83**, 036206 (2011).
[25] R. Fonseca, U. V. Nägerl, R. G. M. Morris, and T. Bonhoeffer, Neuron **44**, 1011 (2004).
[26] S. Royer and D. Pare, Nature (London) **422**, 518 (2003).
[27] C. Xu, X. Tang, H. Lü, K. Alfaro-Bittner, S. Boccaletti, M. Perc, and S. Guan, Phys. Rev. Res. **3**, 043004 (2021).
[28] W. Zou and J. Wang, Phys. Rev. E **102**, 012219 (2020).
[29] G. Filatrella, N. F. Pedersen, and K. Wiesenfeld, Phys. Rev. E **75**, 017201 (2007).
[30] P. Rajwani, A. Suman, and S. Jalan, Chaos **33**, 061102 (2023).
[31] C. Wang and N. B. Garnier, Chaos **26**, 113119 (2016).
[32] M. Kumar and S. Gupta, Phys. Rev. E **106**, 044310 (2022).
[33] E. Ott and T. M. Antonsen, Chaos **18**, 037113 (2008).
[34] E. Ott and T. M. Antonsen, Chaos **19**, 023117 (2009).
[35] P. S. Skardal and C. Xu, Chaos **32**, 053120 (2022).
[36] H. Bi, X. Hu, S. Boccaletti, X. Wang, Y. Zou, Z. Liu, and S. Guan, Phys. Rev. Lett. **117**, 204101 (2016).
[37] C. Xu, S. Boccaletti, S. Guan, and Z. Zheng, Phys. Rev. E **98**, 050202(R) (2018).